Article

Tuning commensurability in twisted van der Waals bilayers

https://doi.org/10.1038/s41586-023-06904-w

Received: 26 March 2023

Accepted: 28 November 2023

Published online: 17 January 2024

Check for updates

Yanxing Li[1,7], Fan Zhang[1,7], Viet-Anh Ha[1,2], Yu-Chuan Lin[3,4], Chengye Dong[3], Qiang Gao[1], Zhida Liu[1], Xiaohui Liu[1], Sae Hee Ryu[5], Hyunsue Kim[1], Chris Jozwiak[5], Aaron Bostwick[5], Kenji Watanabe[6], Takashi Taniguchi[6], Bishoy Kousa[1], Xiaoqin Li[1], Eli Rotenberg[5], Eslam Khalaf[1], Joshua A. Robinson[3], Feliciano Giustino[1,2] & Chih-Kang Shih[1]✉

Moiré superlattices based on van der Waals bilayers[1–4] created at small twist angles lead to a long wavelength pattern with approximate translational symmetry. At large twist angles (θ_t), moiré patterns are, in general, incommensurate except for a few discrete angles. Here we show that large-angle twisted bilayers offer distinctly different platforms. More specifically, by using twisted tungsten diselenide bilayers, we create the incommensurate dodecagon quasicrystals at $\theta_t = 30°$ and the commensurate moiré crystals at $\theta_t = 21.8°$ and 38.2°. Valley-resolved scanning tunnelling spectroscopy shows disparate behaviours between moiré crystals (with translational symmetry) and quasicrystals (with broken translational symmetry). In particular, the K valley shows rich electronic structures exemplified by the formation of mini-gaps near the valence band maximum. These discoveries demonstrate that bilayers with large twist angles offer a design platform to explore moiré physics beyond those formed with small twist angles.

The emergence of moiré superlattices (MSL) designed in van der Waals (vdW) bilayers has created opportunities to engineer two-dimensional electronic materials with unique properties[1–22]. Thus far, most superlattices investigated are vdW bilayers with small twist angles. At small angles, the moiré wavelength is long, and the pattern is either commensurate or nearly commensurate with the atomic lattices, thus creating a periodically modulated electronic superlattice. At large twist angles, the moiré pattern is, in general, incommensurate with the atomic lattice except for a few angles[23–26]. The incommensurability disrupts the translational symmetry, and the electronic superlattice is lost. Large-angle moiré structures have been mostly unexplored until the discovery of dodecagonal quasicrystal in 30° twisted bilayer graphene (TBLG) in 2018[27,28]. Although mini-gap formations deep below the Dirac point have been observed using angle-resolved photoelectron spectroscopy (ARPES), the absence of electronic coupling near the Fermi level, E_F, has limited the effect of quasiperiodicity on other physical properties that are governed primarily by states near E_F in a metallic system. For example, quantum Hall effect measurements of 30° TBLG show that the two layers act totally independent[29].

Here we overcome this limitation by using tungsten diselenide (WSe_2) twisted bilayers in which the flatter dispersion makes the effects of quasiperiodicity more pronounced at accessible doping[30,31]. We show that large-angle twisted WSe_2 bilayers offer a platform to explore moiré physics beyond the MSL. We use two modes of scanning tunnelling spectroscopy (STS), constant height and constant current, which enable us to distinguish the momentum space features arising from the K and Γ points. By contrasting the behaviour of large-angle commensurate moiré crystals at $\theta_t = 21.8°$ and $\theta_t = 38.2°$ with the 12-fold symmetric 30° incommensurate moiré quasicrystal, we identify several unique properties of the latter. These include the appearance of several Umklapp scattered K valleys and the existence of a dense set of diffraction spots that preserve the rotational symmetry without the translational symmetry. We are able to resolve signals associated with interlayer Umklapp scatterings up to at least third order suggesting strong interlayer hybridization. For moiré crystals, the new electronic structures are well captured by the first-principle supercell calculations. For moiré quasicrystals, we show that the dense diffraction spots facilitate electron scattering in a manner analogous to a quasi-Bragg plane that couples the Umklapp scattered K valleys and lead to the formation of a dense set of mini-gaps near the valence band maximum (VBM). These two moiré structures exemplify the designer platform enabled at large twist angles.

Umklapp scatterings in moiré quasicrystal

Figure 1a shows the experimental set-up of two models—one representing the dodecagonal quasicrystal formed with $\theta_t = 30°$ and the other the $\sqrt{7} \times \sqrt{7}$ commensurate moiré crystal with $\theta_t = 21.8°$ (see angle determination in Supplementary Fig. 1). Scanning tunnelling microscopy (STM) images (Fig. 1b,c) show the anticipated moiré quasicrystal and the moiré crystal. The corresponding fast Fourier transform (FFT) patterns are shown in Fig. 1d,e. Figure 1d shows a dense set of diffraction spots with rotational symmetry but without translational symmetry, which is a characteristic of the quasicrystal. By contrast,

[1]Department of Physics, The University of Texas at Austin, Austin, TX, USA. [2]Oden Institute for Computational Engineering and Sciences, The University of Texas at Austin, Austin, TX, USA. [3]Department of Materials Science and Engineering, Pennsylvania State University, University Park, PA, USA. [4]Department of Materials Science and Engineering, National Yang Ming Chiao Tung University, Hsinchu, Taiwan. [5]Advanced Light Source, Lawrence Berkeley National Laboratory, Berkeley, CA, USA. [6]Research Center for Materials Nanoarchitectonics, National Institute for Materials Science, Tsukuba, Japan. [7]These authors contributed equally: Yanxing Li, Fan Zhang. ✉e-mail: shih@physics.utexas.edu

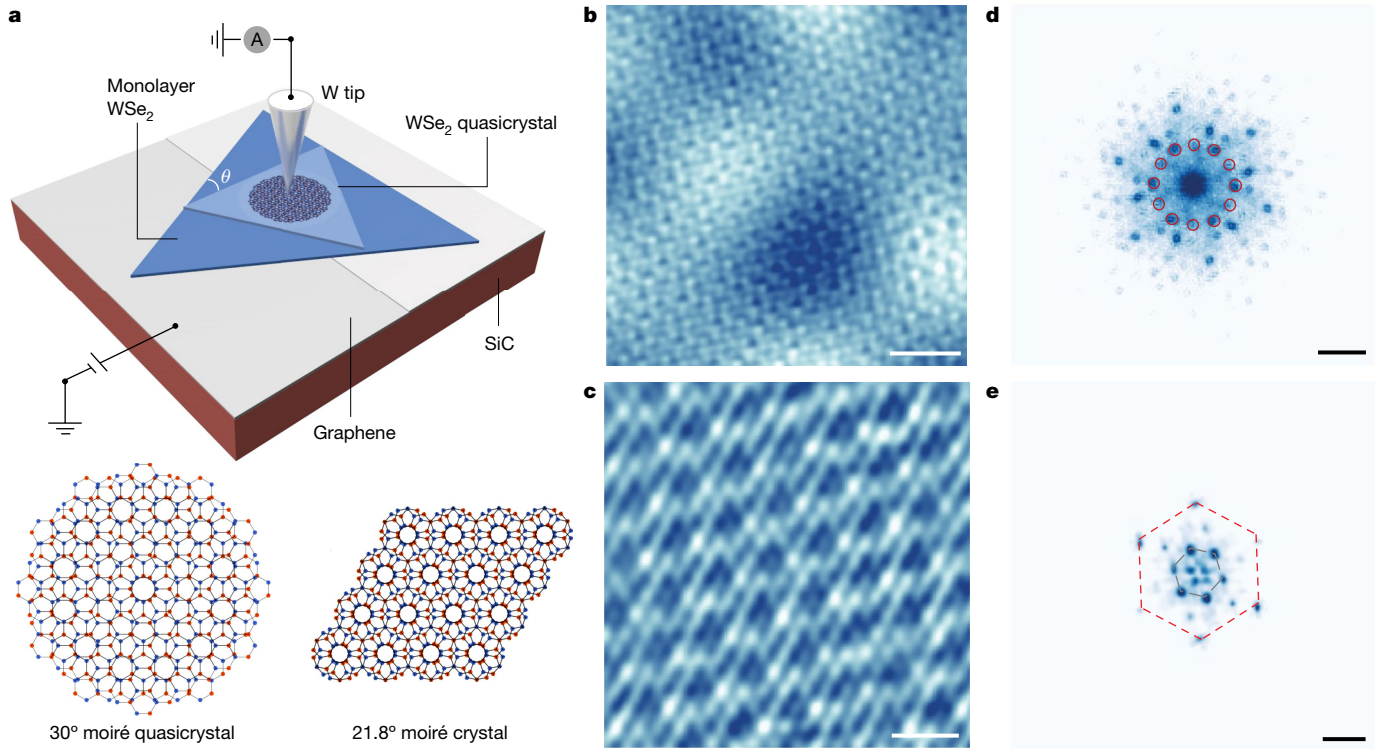

Fig. 1 | WSe_2 commensurate moiré crystal and incommensurate moiré quasicrystal. a, Top: schematic of the experimental set-up. Bottom: the simulated patterns for 30° incommensurate quasicrystal and 21.8° commensurate moiré crystal. **b**, Typical STM topography for 30° incommensurate quasicrystal (V_{Bias} = 0.3 V and I = 30 pA). **c**, Typical STM topography for 21.8° commensurate moiré crystal (V_{Bias} = −0.6 V and I = −20 pA). **d**, The FFT image of the quasicrystal topography in **b** with a six-fold rotational symmetrization. The red circles mark the 12-fold dodecagonal pattern. **e**, The FFT image of the 21.8° commensurate moiré topography in **c** with a six-fold rotational symmetrization. The outer and inner dashed hexagons mark the frequency peaks of the WSe_2 reciprocal lattice vectors for the Bragg lattice and the commensurate moiré crystal, respectively. Scale bars, 2 nm (**b**); 1 nm (**c**); and 2 nm^{-1} (**d**,**e**).

the diffraction spots of the moiré crystal are commensurate with the atomic diffraction spots with a scaling ratio of 1/√7. The dense diffraction spots in Fig. 1d can be analysed by considering the mutual Umklapp scattering between the top and bottom layers, a method previously used for 30° TBLG[27,28] (Supplementary Figs. 2 and 3 and Supplementary Note 1). In our case, up to third-order Umklapp scattering can be identified. As a result, the original K valleys for individual layers are Umklapp scattered, creating a dense distribution of K valleys (Fig. 2a). As discussed below, the electronic coupling of these K valleys endows the rich electronic structures associated with the moiré quasicrystals. The distribution of K valleys in the first quadrant is shown in Fig. 2b, in which we also label three sets of K-valley pairs (in dashed rectangles). For each pair of K valleys, an electronic coupling will open a gap that is at the energy degenerate point (anti-crossing) (Fig. 2c). Figure 2d is the simulated density of states (DOS) near the gap using the two-band coupling model (Supplementary Note 2). Below the gap is a paraboloid local maximum and above the gap is a saddle point that leads to a Van Hove singularity (VHS) with logarithmic divergence in DOS. As a consequence of the dense set of diffraction spots in moiré quasicrystals, there are many K-valley pairs, the couplings of which can lead to anti-crossings and gap openings. We thus expect the formation of many mini-gaps in moiré quasicrystals, which correspond to many VHS in DOS.

Observation of VHS in moiré quasicrystal

The electronic structures are investigated using valley-resolved STS. Two different modes of STS are simultaneously used: (1) the conventional constant-height STS (CHSTS) and (2) the constant-current STS (CCSTS). As discussed previously, the K-valley states rapidly decay into the vacuum (owing to a large $k_{\parallel}$) and are thus difficult to detect using CHSTS. This difficulty in detecting the K-valley states can be overcome using the CCSTS[32]. More detailed descriptions of this method can be found in Supplementary Note 3.

We first discuss the electronic structures for the moiré quasicrystal in Fig. 3. The STM image for the moiré quasicrystal is shown in Fig. 3a with a few spatial locations marked in which the tunnelling spectra are acquired. The experimental condition to observe quasicrystal structure is discussed in Supplementary Fig. 8. Figure 3b shows the spectra acquired using conventional STS. The two prominent peaks correspond to the two split Γ valleys resulting from the interlayer coupling. Here we find $\Delta_{\Gamma-\Gamma}$ = 0.61 eV, which is smaller than the value of 0.75 eV observed in the regular R- or H-stacked bilayers (Supplementary Figs. 9 and 10). The smaller $\Delta_{\Gamma-\Gamma}$ is because of the reduction of Γ–Γ repulsion at a large twist angle. Owing to the rapid decay rate of the K-valley states into the vacuum, they are very difficult to be detected in the CHSTS mode. In the CCSTS mode, as the sample bias is raised above the highest Γ state, the tip-to-sample-distance (Z) is automatically adjusted to a smaller value by the feedback to detect the K-valley states (Fig. 3c). As the bias is raised above the VBM, the Z value is reduced further and the tunnelling occurs between the tip and the bilayer graphene (BLG) substrate. These Z–V plots in the constant current mode delineate different tunnelling regimes (Γ valley, K valley and BLG) from which the VBM can be determined precisely. The fine spectral features in the K valley are shown in the differential conductivity $(\partial I/\partial V)_I$ (Fig. 3d–g). We can identify four sharp spectral features (peaks 1–4) located at 26 meV, 48 meV, 93 meV and 154 meV below the VBM, respectively (Fig. 3d). Among

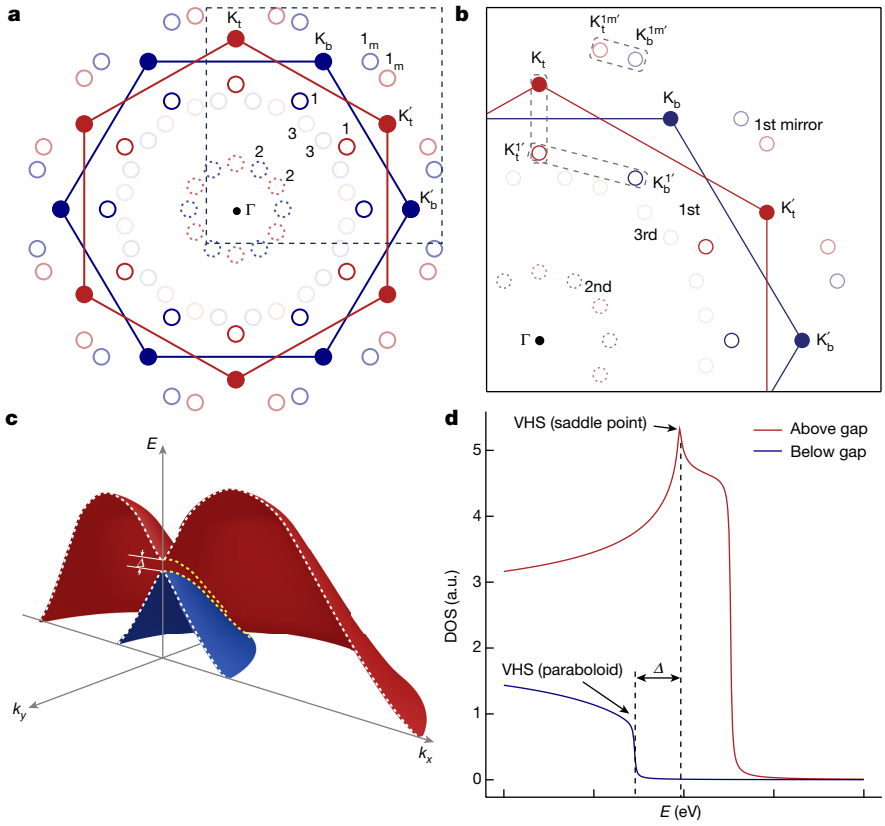

Fig. 2 | Umklapp scatterings and mini-gap formation. a, Schematic of the first three orders of Umklapp scatterings near the first Brillouin zone for the 30° quasicrystal. The red and blue hexagons mark the top and bottom Brillouin zones, respectively. The red dots and circles represent the original K (K′) valleys and Umklapp-scattered K (K′) replicas that originated from the top layers, respectively. The blue dots and circles represent the original K (K′) valleys and Umklapp-scattered K (K′) replicas that originated from the bottom layers, respectively. **b**, The distribution of K valleys in the first quadrant. Three sets of K-valley pairs, in which the couplings can lead to anti-crossings, and gap openings near E_F are marked in dashed rectangles. **c**, Schematic of a three-dimensional band dispersion showing a mini-gap formed by the anti-crossing of the K valleys. The white and yellow dashed lines represent the gapped band structures in k_x and k_y directions in the momentum space, respectively. **d**, Simulated DOS as a function of energy for a typical mini-gap. The top band edge (saddle point) corresponds to a sharp VHS with logarithmic divergence, whereas the bottom edge (paraboloid) corresponds to a weak VHS. a.u., arbitrary units.

them, peaks 1 and 3 have a clear signature of VHS associated with saddle points above the gap, whereas peaks 2 and 4 are interpreted as the VHS of the paraboloid below the gap (for further details, see Supplementary Fig. 11). At other spatial locations (Fig. 3e–g), spectra show similar structures with some sharp peaks that can be identified as saddle points. As another example in Fig. 3f, the two sharp VHS (saddle points) features occur at 36 meV and 100 meV below the VBM and coincide closely with peaks 1 and 3 in Fig. 3d. The observations of these VHS in the tunnelling spectra provide unambiguous signatures for the existence of mini-gaps because of coupled K valleys that are Umklapp scattered. If we further interpret peaks 2 and 4 in Fig. 3d as the energy locations below the gap, we can estimate the energy locations (and sizes) of the mini-gaps at 37 meV (Δ = 22 meV) and 124 meV (Δ = 61 meV) below the VBM, respectively.

We also carried out nano-ARPES on exfoliated and stacked WSe_2 bilayers from which we confirm our valley assignments (Extended Data Fig. 1) and observe the band crossing of K_t and K_b occurring at 0.53 eV below the VBM (Extended Data Fig. 2). Given that the energy-crossing location is directly proportional to Δk^2, where Δk is the separation of the two K valleys in k space, we can estimate the energy locations of the mini-gaps due to coupling of $K_t^{1m'} - K_b^{1m'}$ and $K_t - K_t^{1\prime}$ to be at 36 ± 5 meV and 134 ± 20 meV, respectively, below the VBM (Supplementary Note 4), matching quite well with the experimental observation using STS. The crossing of $K_t^{1\prime} - K_b^{1\prime}$ (at 270 ± 41 meV below VBM) might be too close to the Γ_1 to be visible by STS. More technical details of nano-ARPES investigations are provided in Supplementary Note 5.

Interlayer coherent couplings in moiré crystal

We next discuss the electronic structure of the moiré crystal. The commensurate moiré structures at θ_t = 21.8° and 38.2° have attracted notable interest in recent years, exemplified by the observation of coherent interlayer transport in BLG[33–35] and coherent interlayer excitons in bilayer transition-metal dichalcogenides (TMDs)[36]. Thus far, however, STM and STS investigations are lacking. For BLG, there is no distinction between θ_t = 21.8° and 38.2° because K and K′ are degenerate. For bilayer TMD, the situation is different because the K–K′ degeneracy is lifted.

Figure 4a shows the STM image of a moiré crystal at θ_t = 38.2°. In our investigations, the majority (70%) of commensurate moiré structures are with θ_t = 38.2° and the minority (30%) with θ_t = 21.8°. Moreover, detailed atomic image analysis shows isotropic strain ranging from +2% to −3% for different moiré crystals (Supplementary Note 6). Conventional STS show similar structures as those observed in moiré quasicrystals in which two Γ valleys are observable but not the K valleys (Supplementary Fig. 22), whereas CCSTS (Fig. 4b) shows additional structures above the upper Γ valley. Two clear peaks (peaks 1 and 2), with 60 meV separation are observed near the VBM. Furthermore, a weak shoulder (peak 3) is

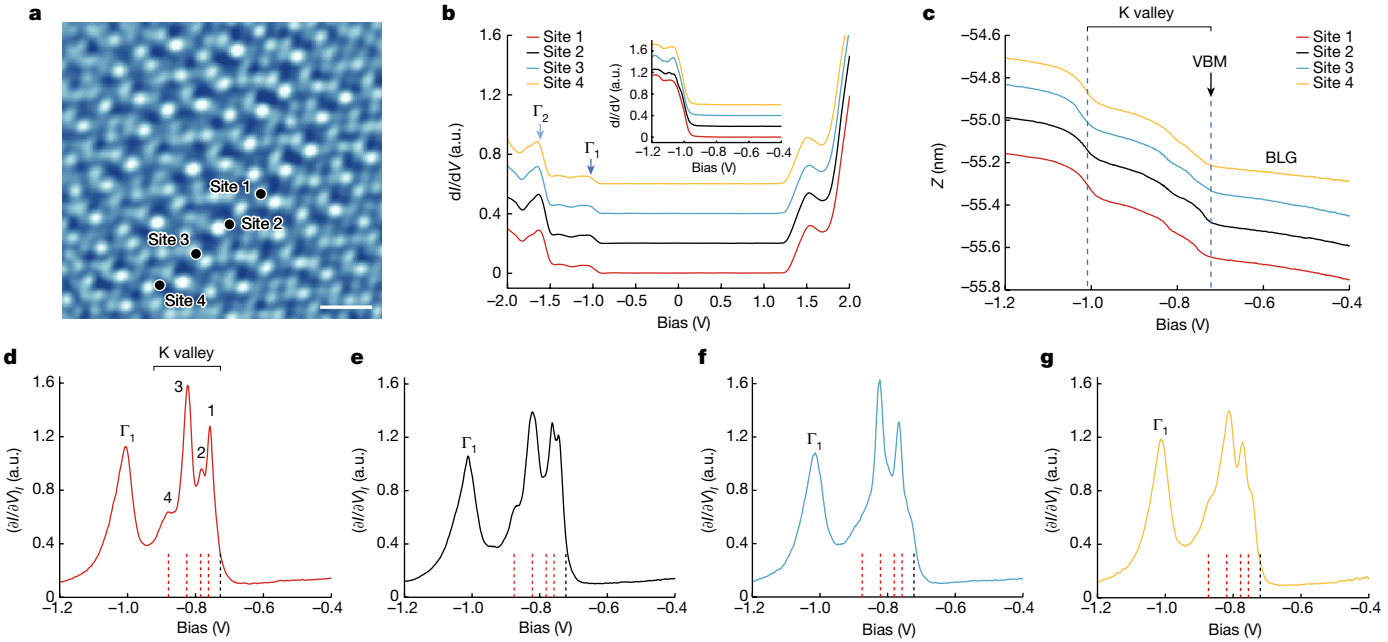

Fig. 3 | Observation of VHS in the 30° moiré quasicrystal. a, STM topography image for a typical 30° quasicrystal region. The black dots mark the sites of the measurement (V_{Bias} = −0.75 V and I = −20 pA). Scale bar, 1 nm. **b**, Large-scale (V_{Bias} = −2.0 V and I = −50 pA) and magnified (inset) regular constant-height dI/dV spectroscopies (V_{Bias} = −1.2 V and I = −200 pA) taken from sites 1–4. The light-blue and blue arrows mark Γ_2 and Γ_1, respectively. **c**, Magnified Z–V spectroscopies from sites 1–4 (I = −30 pA). **d**–**g**, Constant-current $\partial I/\partial V$ spectroscopies from the measurement sites labelled in **a**: site 1 (**d**), site 2 (**e**), site 3 (**f**), site 4 (**g**). All peak (shoulder) locations above Γ_1 are marked by red dashed lines. The location of K_{VBM} is indicated by a black dashed line (V_{int} = −1.2 V, I = −30 pA and V_{amp} = 10 mV).

located at around 60 meV below peak 2. All moiré crystals show very similar spectral features regardless of θ_t = 21.8° (Fig. 4c) or 38.2°. Moreover, we do not observe sharp VHS associated with saddle points.

To aid the interpretation of spectral features, we carried out first-principle density functional theory (DFT) calculations. Figure 4d shows the Brillouin zones for the top layer (red), the bottom layer (blue) and the commensurate moiré structure (purple) for a θ_t = 21.8° (38.2°) bilayer. A few critical points (μ, κ and κ′) in the moiré Brillouin zone (MBZ) are of interest. The two K valleys, K_t and K_b, intersect at the μ point at which the anti-crossing is expected. The DFT calculation shows a gap of about 40 meV opening up at this point, albeit it occurs at an energy level near the Γ_1 state (Fig. 4e and Supplementary Fig. 24). At 21.8°, all K_t valleys are Umklapp scattered to κ′ and all K_b valleys are Umklapp scattered to κ and thus crossing occurs at only the μ point. On the other hand, K_b' and K_t are scattered at the same κ′ point. At 38.2°, however, the converse is true. K_t and K_b' will intersect at μ, whereas K_t and K_b would be scattered at the same κ point. If spin is conserved after Umklapp scattering, then for the θ_t = 38.2° bilayer, we do not expect anti-crossing to occur at μ, but a K–K splitting at κ. DFT calculations for the θ_t = 38.2° bilayer confirm the diminishing gap at μ, but only a small K–K splitting (2 meV) at κ (Supplementary Fig. 25). Experimental investigations in regular bilayers, nevertheless, show notable interlayer K–K coupling[37–40]. Moreover, in $MoSe_2/WS_2$ heterobilayers, splitting of moiré exciton states is found near both commensurate angles, indicating that coherent coupling exists for both K_t– K_b and K_t–K_b' (refs. 10,41). Another evidence for the K–K′ coupling is found in the quasiparticle interference analysis (Supplementary Note 7). This mechanism explains the observation of a double-peak structure near the VBM for both twisting angles. Moreover, it indicates that anti-crossing can also exist for both angles, albeit the energy location is too close to the Γ point to be observed by STS. Then the weak shoulder (peak 3) could be interpreted as the remanent of the VHS (saddle point) above the Γ.

In summary, we have studied twisted WSe_2 bilayers at large twist angles and discovered distinct behaviour of incommensurate 12-fold rotationally symmetric 30° moiré quasicrystals and commensurate moiré crystals at 21.8° and 38.2°. The former features an aperiodic long-range order that yields a dense set of diffraction spots in the k space. By combining the constant-height and constant-current STM signals, we can resolve the spectral features arising from the K and Γ points. We observe the VHS signatures originating from several mini-gaps in the quasiperiodic structure that can be explained using a coupled K-valley model with up to third-order Umklapp scattering suggesting strong interlayer coupling. For the commensurate 21.8° (38.2°) structure, two points in the MBZ are of interest: anti-crossing at the μ point and the coherent coupling at κ point. The absence of VHS and the double-peak structure near the VBM can be interpreted as a manifestation of band structures in commensurate moiré crystals. In contrast to the previously studied 30° TBLG, the flatter dispersion of our system leads to stronger interlayer coupling at a smaller bias voltage making it a very promising platform to study the physics of moiré quasicrystals at finite doping. Moreover, the crystallographically forbidden 12-fold rotation symmetry makes our system distinct from the quasiperiodic multilayer moiré systems with multiple unrelated twist angle[42]. Moreover, TMD-based moiré quasicrystals is a semiconductor system with strong spin–orbit coupling that endows a rich interplay of valley and spin degrees of freedom that affect both optical and transport properties. The theoretical analysis further shows that such moiré quasicrystals can be generalized to multilayer structures with higher rotational symmetry in which the quasiperiodic interlayer coupling can be brought down in energy even further. For example, using trilayers with two consecutive 20° twists, a previously unknown type of quasicrystal with 18-fold rotational symmetry and with an even denser set of diffraction patterns in which the mini-gaps are expected to occur at smaller doping (Supplementary Fig. 29). This work provides a proof of concept for using large-twist-angle vdW structures as a design platform to explore moiré physics beyond those formed at small twist angles.

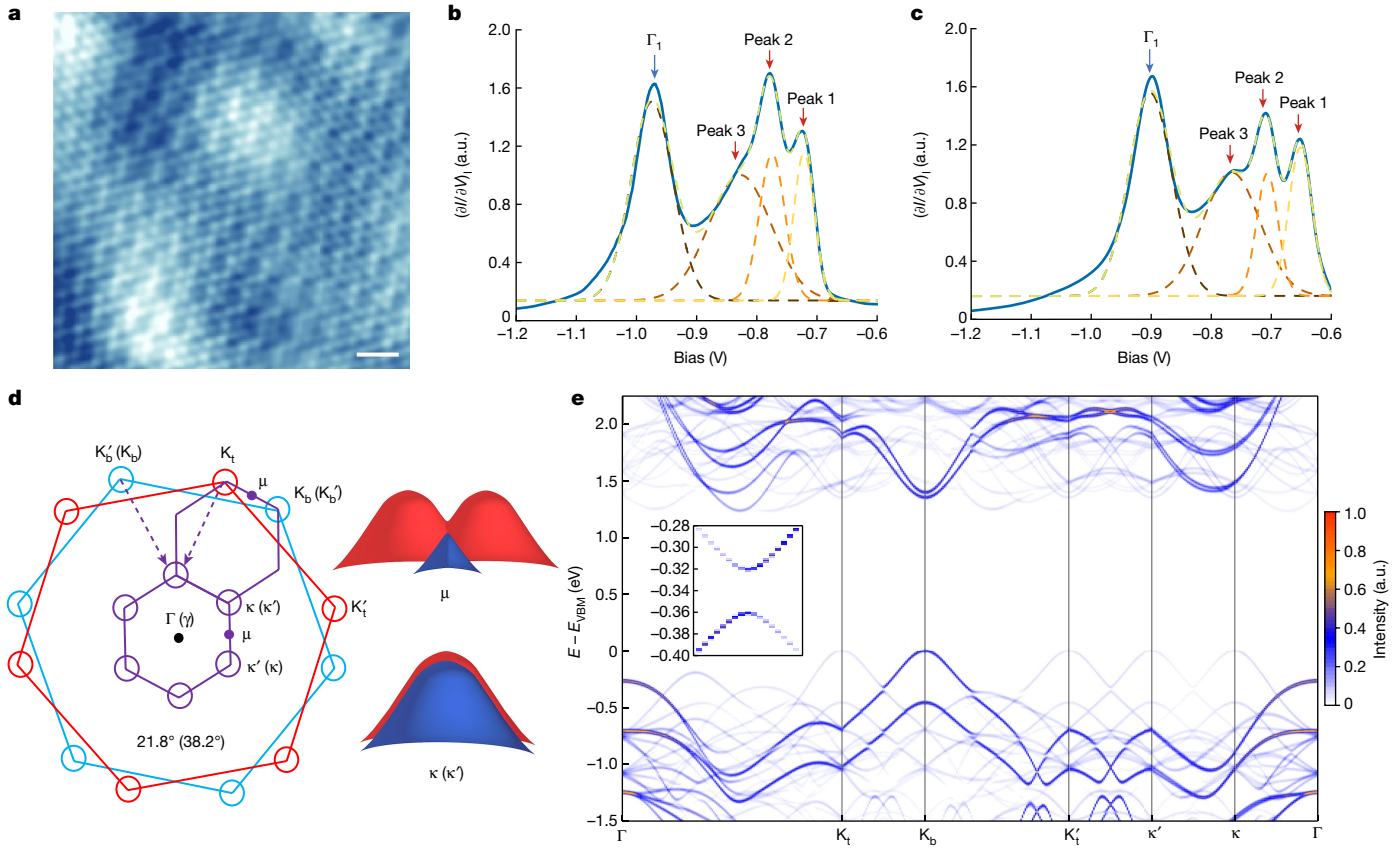

Fig. 4 | Interlayer couplings in 21.8° and 38.2° commensurate moiré crystal. **a**, STM topography image for a typical 38.2° commensurate moiré crystal region (V_{Bias} = −0.5 V and I = −20 pA). Scale bar, 1 nm. **b**, Gaussian peak fittings for magnified constant-current $\partial I/\partial V$ spectroscopies at the 38.2° twisted region. The dashed curves represent the fitted peaks (V_{int} = −1.2 V, I = −20 pA and V_{amp} = 15 mV). **c**, Gaussian peak fittings for magnified constant-current $\partial I/\partial V$ spectroscopies at the 21.8° twisted region. The dashed curves represent the fitted peaks (V_{int} = −1.2 V, I = −20 pA and V_{amp} = 15 mV). **d**, Left: schematic showing the first Brillouin zones for 21.8° (38.2°) twisted WSe_2 bilayer. The purple, red and black hexagons mark the moiré, top-layer and bottom-layer Brillouin zones, respectively. The K_t (K_t') and K_b (K_b') points of the top- and bottom-layer Brillouin zone are, respectively, marked with red and blue circles, and the κ (κ′) points are marked with purple circles. Right: schematics showing the anti-crossing coupling at μ and the coherent coupling at κ (κ′). **e**, DFT-calculated unfolded band structure of 21.8° commensurate moiré along the k-space path: Γ − K_t − K_b − K_t' − κ′ − κ − Γ. Inset: the magnified band structure of K_t and K_b band crossing showing the mini-gap.

Online content

Any methods, additional references, Nature Portfolio reporting summaries, source data, extended data, supplementary information, acknowledgements, peer review information; details of author contributions and competing interests; and statements of data and code availability are available at https://doi.org/10.1038/s41586-023-06904-w.

1. Bistritzer, R. & MacDonald, A. H. Moiré bands in twisted double-layer graphene. *Proc. Natl Acad. Sci. USA* **108**, 12233–12237 (2011).
2. Zhang, C. et al. Interlayer couplings, Moiré patterns, and 2D electronic superlattices in MoS_2/WSe_2 hetero-bilayers. *Sci. Adv.* **3**, e1601459 (2017).
3. Cao, Y. et al. Correlated insulator behaviour at half-filling in magic-angle graphene superlattices. *Nature* **556**, 80–84 (2018).
4. Cao, Y. et al. Unconventional superconductivity in magic-angle graphene superlattices. *Nature* **556**, 43–50 (2018).
5. Jin, C. et al. Observation of moiré excitons in WSe_2/WS_2 heterostructure superlattices. *Nature* **567**, 76–80 (2019).
6. Tran, K. et al. Evidence for moiré excitons in van der Waals heterostructures. *Nature* **567**, 71–75 (2019).
7. Seyler, K. L. et al. Signatures of moiré-trapped valley excitons in $MoSe_2$/WSe_2 heterobilayers. *Nature* **567**, 66–70 (2019).
8. Lu, X. et al. Superconductors, orbital magnets and correlated states in magic-angle bilayer graphene. *Nature* **574**, 653–657 (2019).
9. Zhang, Z. et al. Flat bands in twisted bilayer transition metal dichalcogenides. *Nat. Phys.* **16**, 1093–1096 (2020).
10. Zhang, L. et al. Twist-angle dependence of moiré excitons in WS_2/$MoSe_2$ heterobilayers. *Nat. Commun.* **11**, 5888 (2020).
11. Wang, L. et al. Correlated electronic phases in twisted bilayer transition metal dichalcogenides. *Nat. Mater.* **19**, 861–866 (2020).
12. Xie, Y. et al. Fractional Chern insulators in magic-angle twisted bilayer graphene. *Nature* **600**, 439–443 (2021).
13. Li, H. et al. Imaging moiré flat bands in three-dimensional reconstructed WSe_2/WS_2 superlattices. *Nat. Mater.* **20**, 945–950 (2021).
14. Bai, Y. et al. Excitons in strain-induced one-dimensional moiré potentials at transition metal dichalcogenide heterojunctions. *Nat. Mater.* **19**, 1068–1073 (2020).
15. Sharpe, A. L. et al. Emergent ferromagnetism near three-quarters filling in twisted bilayer graphene. *Science* **365**, 605–608 (2019).
16. Oh, M. et al. Evidence for unconventional superconductivity in twisted bilayer graphene. *Nature* **600**, 240–245 (2021).
17. Li, T. et al. Quantum anomalous Hall effect from intertwined moiré bands. *Nature* **600**, 641–646 (2021).
18. Choi, Y. et al. Correlation-driven topological phases in magic-angle twisted bilayer graphene. *Nature* **589**, 536–541 (2021).
19. Wang, X. et al. Interfacial ferroelectricity in rhombohedral-stacked bilayer transition metal dichalcogenides. *Nat. Nanotechnol.* **17**, 367–371 (2022).
20. Törmä, P., Peotta, S. & Bernevig, B. A. Superconductivity, superfluidity and quantum geometry in twisted multilayer systems. *Nat. Rev. Phys.* **4**, 528–542 (2022).
21. Weston, A. et al. Interfacial ferroelectricity in marginally twisted 2D semiconductors. *Nat. Nanotechnol.* **17**, 390–395 (2022).
22. Rozhkov, A. V., Sboychakov, A. O., Rakhmanov, A. L. & Nori, F. Electronic properties of graphene-based bilayer systems. *Phys. Rep.* **648**, 1–104 (2016).
23. Lopes dos Santos, J. M. B., Peres, N. M. R. & Castro Neto, A. H. Continuum model of the twisted graphene bilayer. *Phys. Rev. B* **86**, 155449 (2012).
24. Mele, E. J. Commensuration and interlayer coherence in twisted bilayer graphene. *Phys. Rev. B* **81**, 161405 (2010).
25. Sboychakov, A. O., Rakhmanov, A. L., Rozhkov, A. V. & Nori, F. Electronic spectrum of twisted bilayer graphene. *Phys. Rev. B* **92**, 075402 (2015).
26. Rozhkov, A. V., Sboychakov, A. O., Rakhmanov, A. L. & Nori, F. Single-electron gap in the spectrum of twisted bilayer graphene. *Phys. Rev. B* **95**, 045119 (2017).

27. Ahn, S. J. et al. Dirac electrons in a dodecagonal graphene quasicrystal. *Science* **361**, 782–786 (2018).
28. Yao, W. et al. Quasicrystalline 30° twisted bilayer graphene as an incommensurate superlattice with strong interlayer coupling. *Proc. Natl Acad. Sci. USA* **115**, 6928–6933 (2018).
29. Pezzini, S. et al. 30°-twisted bilayer graphene quasicrystals from chemical vapor deposition. *Nano Lett.* **20**, 3313–3319 (2020).
30. Nguyen, P. V. et al. Visualizing electrostatic gating effects in two-dimensional heterostructures. *Nature* **572**, 220–223 (2019).
31. Bisri, S. Z., Shimizu, S., Nakano, M. & Iwasa, Y. Endeavor of iontronics: from fundamentals to applications of ion-controlled electronics. *Adv. Mater.* **29**, 1607054 (2017).
32. Zhang, C. et al. Probing critical point energies of transition metal dichalcogenides: surprising indirect gap of single layer WSe_2. *Nano Lett.* **15**, 6494–6500 (2015).
33. Koren, E. et al. Coherent commensurate electronic states at the interface between misoriented graphene layers. *Nat. Nanotechnol.* **11**, 752–757 (2016).
34. Inbar, A. et al. The quantum twisting microscope. *Nature* **614**, 682–687 (2023).
35. Chari, T., Ribeiro-Palau, R., Dean, C. R. & Shepard, K. Resistivity of rotated graphite–graphene contacts. *Nano Lett.* **16**, 4477–4482 (2016).
36. Zhao, X. et al. Strong moiré excitons in high-angle twisted transition metal dichalcogenide homobilayers with robust commensuration. *Nano Lett.* **22**, 203–210 (2022).
37. Weston, A. et al. Atomic reconstruction in twisted bilayers of transition metal dichalcogenides. *Nat. Nanotechnol.* **15**, 592–597 (2020).
38. McCreary, K. M. et al. Stacking-dependent optical properties in bilayer WSe_2. *Nanoscale* **14**, 147–156 (2022).
39. Hsu, W.-T. et al. Quantitative determination of interlayer electronic coupling at various critical points in bilayer MoS_2. *Phys. Rev. B* **106**, 125302 (2022).
40. Hsu, W.-T. et al. Tailoring excitonic states of van der Waals bilayers through stacking configuration, band alignment, and valley spin. *Sci. Adv.* **5**, eaax7407 (2019).
41. Zhang, Y., Devakul, T. & Fu, L. Spin-textured Chern bands in AB-stacked transition metal dichalcogenide bilayers. *Proc. Natl Acad. Sci. USA* **118**, e2112673118 (2021).
42. Uri, A. et al. Superconductivity and strong interactions in a tunable moiré quasicrystal. *Nature* **620**, 762–767 (2023).

Methods

Sample growth

High-quality buffer on SiC was synthesized using a two-step process. First, the monolayer epitaxial graphene was synthesized using silicon sublimation from the Si face of the semi-insulating SiC substrates (II–VI). Before the growth, the SiC substrates were annealed in 10% hydrogen (balance argon) at 1,500 °C for 30 min to remove subsurface damages due to chemical and mechanical polishing. Then monolayer epitaxial graphene (MLEG) was formed at 1,800 °C for 30 min in a pure argon atmosphere. Second, an Ni stressor layer was used to exfoliate the top graphene layer to obtain fresh and high-quality buffer on SiC. After this, 270 nm of Ni was e-beam deposited on MLEG at a rate of 5 Å s^{-1} as a stressor layer. Then a thermal release tape was used to peel off the top graphene layer from the substrate. The growth of WSe_2 crystals on an epitaxial graphene substrate was carried out at 800 °C in a custom-built vertical cold-wall chemical vapour deposition (CVD) reactor for 20 min (ref. 43). The tungsten hexacarbonyl ($W(CO)_6$) (99.99%, Sigma-Aldrich) source was kept inside a stainless-steel bubbler in which the temperature and pressure of the bubbler were always held at 37 °C and 730 torr, respectively. Mass-flow controllers were used to supply H_2 carrier gas to the bubbler to transport the $W(CO)_6$ precursor into the CVD chamber. The flow rate of the H_2 gas through the bubbler was maintained at a constant 8 standard cubic centimetres per minute (sccm), which resulted in a $W(CO)_6$ flow rate of 9.0×10^{-4} sccm at the outlet of the bubbler. H_2Se (99.99%, Matheson) gas was supplied from a separate gas manifold and introduced at the inlet of the reactor at a constant flow rate of 30 sccm.

STM and STS measurements

STM and STS measurements were conducted at 4.3 K in the STM chamber, with a base pressure of about 10^{-11} torr. The W tip was prepared by electrochemical etching and then cleaned by in situ electron-beam heating. STM d*I*/d*V* spectra were measured using a standard lock-in technique, for which the modulation frequency was 758 Hz. Two different modes of STS were simultaneously used: (1) the conventional constant-height STS and (2) the constant-current STS.

Sample fabrication for nano-ARPES measurements

The WSe_2 monolayers, bilayers and hBN layers were exfoliated from high-quality bulk crystals. We used the tear-and-stack method to control the twist angle with an accuracy of more than 0.1°. The thickness of the bottom hBN layers in all samples was around 3 nm, according to the atomic force microscopy measurements. All samples were first annealed at 300 °C in a molecular-beam epitaxy chamber for 30 min with sufficient Se pressure and then annealed at 250 °C in an ultrahigh vacuum (about 1×10^{-10} torr) chamber before the ARPES measurement.

nano-ARPES measurements

The experimental set-up used in this study involved the implementation of nano-ARPES to investigate the electronic structure of the sample. The nano-ARPES measurements were conducted at the MAESTRO beamline at the Advanced Light source. A capillary mirror obtained from Sigray was used to achieve a beam size of approximately 1 μm. The measurements were performed at a temperature of approximately 20 K with the R4000 analyser, equipped with a custom electron deflector, and a photon energy of 150 eV was used during the experiments. To identify the target region, XY scans were conducted with a step size of 0.5 μm. The thickness and the rotation angle of the sample were determined by comparing the intensity of the core-level spectrum of O 2s obtained from the natively oxidized silicon substrate and the valence band structure of the sample.

Theoretical calculation

The density functional theory calculations were implemented in the Quantum ESPRESSO suite[44,45]. We used the Perdew–Burke–Ernzerhof exchange-correlation functional[46] in all density functional theory calculations. The structural optimization was obtained with the criteria for force less than 0.025 eV $Å^{-1}$, pressure less than 0.5 kbar and total energy less than 0.0014 eV. We used optimized norm-conserving pseudopotentials[47] from the PseudoDojo library[48] with plane waves kinetic energy cutoff of 98 Ry as recommended. The vdW interaction was taken into account within the semiempirical approach Grimme-D3 (ref. 49). The spin–orbit coupling was also included. The unfolded band structures were performed using the BandUP code[50–52].

Data availability

Source data that reproduce the plots in the main text and extended data figures are provided with this paper. Source data that reproduce the plots in the Supplementary Information are available on request.

Code availability

The DFT calculations presented in the paper were carried out using publicly available electronic structure codes (referenced in Methods). All other codes in the Supplementary Information are available upon reasonable request.

43. Lin, Y.-C. et al. Realizing large-scale, electronic-grade two-dimensional semiconductors. *ACS Nano* **12**, 965–975 (2018).
44. Giannozzi, P. et al. Quantum ESPRESSO: a modular and open-source software project for quantum simulations of materials. *J. Phys. Condens. Matter* **21**, 395502 (2009).
45. Giannozzi, P. et al. Advanced capabilities for materials modelling with Quantum ESPRESSO. *J. Phys. Condens. Matter* **29**, 465901 (2017).
46. Perdew, J. P., Burke, K. & Ernzerhof, M. Generalized gradient approximation made simple. *Phys. Rev. Lett.* **77**, 3865–3868 (1996).
47. Hamann, D. R. Optimized norm-conserving Vanderbilt pseudopotentials. *Phys. Rev. B* **88**, 085117 (2013).
48. van Setten, M. J. et al. The PseudoDojo: training and grading a 85 element optimized norm-conserving pseudopotential table. *Comput. Phys. Commun.* **226**, 39–54 (2018).
49. Grimme, S., Antony, J., Ehrlich, S. & Krieg, H. A consistent and accurate ab initio parametrization of density functional dispersion correction (DFT-D) for the 94 elements H–Pu. *J. Chem. Phys.* **132**, 154104 (2010).
50. Medeiros, P. V. C., Stafström, S. & Björk, J. Effects of extrinsic and intrinsic perturbations on the electronic structure of graphene: retaining an effective primitive cell band structure by band unfolding. *Phys. Rev. B* **89**, 041407 (2014).
51. Medeiros, P. V. C., Tsirkin, S. S., Stafström, S. & Björk, J. Unfolding spinor wave functions and expectation values of general operators: introducing the unfolding-density operator. *Phys. Rev. B* **91**, 041116 (2015).
52. Iraola, M. et al. IrRep: symmetry eigenvalues and irreducible representations of ab initio band structures. *Comput. Phys. Commun.* **272**, 108226 (2022).

Acknowledgements This work was primarily supported by the NSF through the Center for Dynamics and Control of Materials: an NSF Materials Research Science and Engineering Center under cooperative agreement nos. DMR-1720595, DMR-2308817 and the US Air Force grant no. FA2386-21-1-4061. Other supports were from NSF grant nos. DMR-1808751 and DMR-2219610 and the Welch Foundation F-2164. V.-A.H. and F.G. were supported by the Welch Foundation (grant no. F-2139–20230405) and the National Science Foundation (grant no. 2103991). V.-A.H. and F.G. used the resources of the National Energy Research Scientific Computing Center and the Argonne Leadership Computing Facility, which are DOE Office of Science User Facilities supported by the Office of Science of the US Department of Energy (DOE) (contract nos. DE-AC02-05CH11231 and DE-AC02-06CH11357, respectively). V.-A.H. and F.G. acknowledge the Texas Advanced Computing Center (TACC) at The University of Texas at Austin for providing access to Frontera, Lonestar6 and Texascale Days, which contributed to the research results reported in this paper (http://www.tacc.utexas.edu). Work at Penn State University was supported by the Penn State Center for Nanoscale Science (NSF grant no. DMR-2011839) and the Penn State 2DCC-MIP (NSF grant no. DMR-1539916). Y.-C.L. acknowledges the support from the Center for Emergent Functional Matter Science (CEFMS) of NYCU and the Yushan Young Scholar Program from the Ministry of Education of Taiwan. E.R. and S.H.R. acknowledge the funding of the QSA, supported by the US DOE, Office of Science, National Quantum Information Science Research Centers. This research used the resources of the Advanced Light Source, which is a DOE, Office of Science User Facility (contract no. DE-AC02-05CH11231). Z.L., X. Liu and X. Li acknowledge support from the National Science Foundation (NSF grant no. ECCS-2130552), the DOE, Office of Basic Energy Sciences (grant no. DE-SC0019398) and the Welch Foundation (grant no. F-1662). K.W. and T.T. acknowledge support from the JSPS KAKENHI (grant nos. 20H00354, 21H05233 and 23H02052) and the World Premier International Research Center Initiative (WPI), NEXT, Japan.

Author contributions C.-K.S. conceived the experiment. Y.L. and F.Z. carried out the STM and STS measurements. V.-A.H. and F.G. performed the DFT calculations. Y.-C.L. synthesized the twisted WSe_2 bilayers. C.D. prepared the graphitic buffer layer/SiC. J.A.R. supervised the sample preparation effort. H.K. helped anneal the sample and perform the low-energy electron diffraction measurements. Q.G., B.K. and E.K. performed the theoretical model

calculations. Z.L. and X. Liu prepared the exfoliated the sample. X. Li was involved in the discussion. K.W. and T.T. synthesized the hBN bulk crystals. S.H.R. and E.R. performed the nano-ARPES measurement and analysed the ARPES data. C.J. and A.B. helped with the nano-ARPES set-up. Y.L., F.Z. and C.-K.S. analysed the STM data. Y.L., F.Z. and C.-K.S. wrote the paper with contributions from all the authors.

Competing interests The authors declare no competing interests.

Additional information

Supplementary information The online version contains supplementary material available at https://doi.org/10.1038/s41586-023-06904-w.

Correspondence and requests for materials should be addressed to Chih-Kang Shih.

Peer review information *Nature* thanks Shengjun Yuan and the other, anonymous, reviewer(s) for their contribution to the peer review of this work.

Reprints and permissions information is available at http://www.nature.com/reprints.

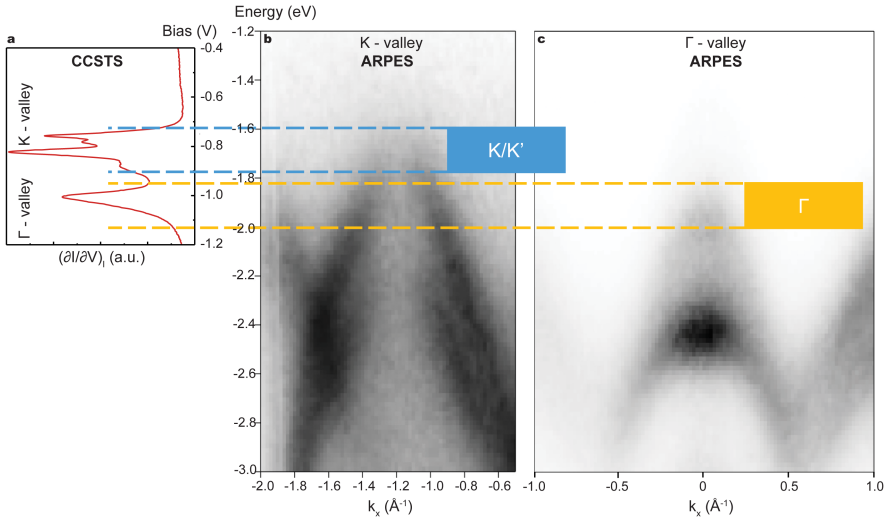

Extended Data Fig. 1 | Comparison of valley assignments between CCSTS and nano-ARPES. a, The zoom-in CCSTS taken on quasicrystal. (same as Fig. 3d) **b**, The zoom in K-valley spectrum from the nano-ARPES measurements. **c**, The zoom in Γ-valley spectrum from the nano-ARPES measurements.

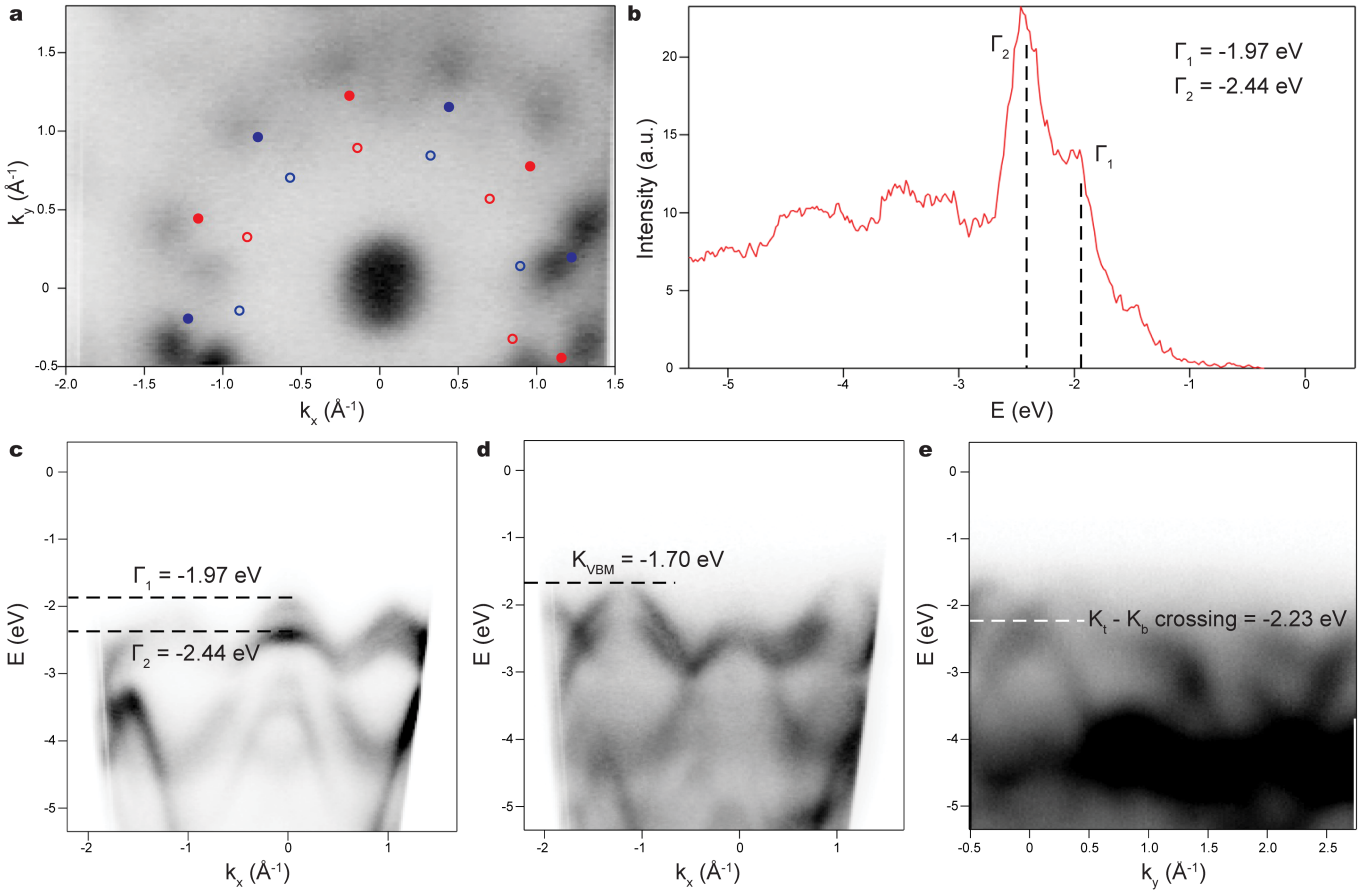

Extended Data Fig. 2 | nano-ARPES results for quasicrystal. a, The constant energy surface at $E = -1.9$ eV. The trigonal K-valleys are labeled by the blue and red solid dots. The blue and red hole circles label the expected locations of the 1st-order Umklapp scatterings. However, no clear features of Umklapp replicas are observed. **b**, Energy distribution curve (EDC) at the Γ. Two peaks represent Γ_1 (−1.97 eV) and Γ_2 (−2.44 eV) respectively. **c**, The measured band structure across the Γ ($k_y = 0$ Å^{-1}). **d**, The measured band structure across the K ($k_y = -0.4$ Å^{-1}), the K_{VBM} is estimated to be at −1.7 eV. **e**, The measured band structure along the K_t-K_b direction ($k_x = -1.4$ Å^{-1}) shows the bands crossing. The energy level of the crossing point is determined by the saddle point, at $E = -2.23$ eV.